PERGAMON

Journal of Quantitative Spectroscopy & Radiative Transfer 78 (2003) 381–407

Journal of Quantitative Spectroscopy & Radiative Transfer

www.elsevier.com/locate/jqsrt

Modelling of atmospheric mid-infrared radiative transfer: the AMIL2DA algorithm intercomparison experiment

T. von Clarmann[a,*], M. Höpfner[a], B. Funke[b], M. López-Puertas[b], A. Dudhia[c], V. Jay[c], F. Schreier[d], M. Ridolfi[e], S. Ceccherini[f], B.J. Kerridge[g], J. Reburn[g], R. Siddans[g]

[a] *Institut für Meteorologie und Klimaforschung (IMK), Forschungszentrum Karlsruhe, Hermann-von-Helmholtz-Platz 1, Eggenstein-Leopoldshafen 76344, Germany*

[b] *Instituto de Astrofisica de Andalucia CSIC, Apartado Postal 3004, Granada 18080, Spain*

[c] *Oxford University, Atmospheric, Oceanic and Planetary Physics, Clarendon Laboratory, Parks Road, Oxford OX1 3PU, UK*

[d] *Deutsches Zentrum für Luft und Raumfahrt, Institut für Methodik der Fernerkundung, Oberpfaffenhofen, D-82234 Wessling, Germany*

[e] *Bologna University, Via Risorgimento 4, 40136 Bologna, Italy*

[f] *Istituto di Fisica Applicata "Nello Carrara", CNR, Via Panciatichi, 64, 50127 Firenze, Italy*

[g] *Rutherford Appleton Laboratory, Chilton, Didcot, Oxfordshire OX11 0QX, UK*

Received 14 June 2002; accepted 1 October 2002

Abstract

When retrieving atmospheric parameters from radiance spectra, the forward modelling of radiative transfer through the Earth's atmosphere plays a key role, since inappropriate modelling directly maps on to the retrieved state parameters. In the context of pre-launch activities of the Michelson Interferometer for Passive Atmospheric Sounding (MIPAS) experiment, which is a high resolution limb emission sounder for measurement of atmospheric composition and temperature, five scientific groups intercompared their forward models within the framework of the Advanced MIPAS Level 2 Data Analysis (AMIL2DA) project. These forward models have been developed, or, in certain respects, adapted in order to be used as part of the groups' MIPAS data processing. The following functionalities have been assessed: the calculation of line strengths including non-local thermodynamic equilibrium, the evaluation of the spectral line shape, application of chi-factors and semi-empirical continua, the interpolation of pre-tabulated absorption cross sections in pressure and temperature, line coupling, atmospheric ray tracing, the integration of the radiative transfer equation through an

* Corresponding author. Fax: +49-7247-824742.
E-mail address: thomas.clarmann@imk.fzk.de (T.von Clarmann).

0022-4073/03/$ - see front matter
PII: S0022-4073(02)00262-5

inhomogeneous atmosphere, the convolution of monochromatic spectra with an instrument line shape function, and the integration of the incoming radiances over the instrument field of view.

Keywords: Infrared radiative transfer; Forward problem; Line-by-line modelling

1. Introduction

The Michelson Interferometer for Passive Atmospheric Sounding (MIPAS) [1–3] on the Envisat Earth observation satellite developed by the European Space Agency (ESA) is a mid-infrared limb emission sounder which provides vertical profiles of atmospheric species relevant to several inter-linked problems in ozone chemistry and global change. Routine data analysis under ESA responsibility covers only six the so-called key species (H_2O, O_3, N_2O, CH_4, HNO_3, NO_2) as well as pressure and temperature. The MIPAS data, however, contain much more information on further atmospheric trace species of very high scientific value. Thus, exploitation of MIPAS data with respect to (a) the retrieval of many more species relevant to atmospheric research such as the complete nitrogen family, chlorine source gases and reservoirs, greenhouse gases, ozone precursors, aerosols, etc., and (b) the retrieval of key species abundance profiles by methods of higher sophistication than affordable under near real time processing constraints are of high interest for better understanding of ozone chemistry and global change. In order to support the development and characterization of methods and tools for this extended analysis of MIPAS data, the project AMIL2DA (Advanced MIPAS Level 2 Data Analysis) has been initiated.

When atmospheric parameters are retrieved from atmospheric radiance spectra, accurate forward modelling of radiative transfer through the Earth's atmosphere is of particular importance, since forward modelling errors directly map on to the retrieved quantities. Intercomparison studies are a standard approach to assess the reliability of radiative transfer models [4–6]. Hence, a major component of the AMIL2DA project is the comparison of the radiative transfer (forward) models used by each group for their retrievals.

2. Theory

Disregarding scattering, which is justified in many applications of infrared remote sensing, the monochromatic radiative transfer equation [7] can be written as

$$L_\nu = L_{0,\nu}\tau_\nu(l_{\mathrm{obs}},0) + \int_{l=0}^{l_{\mathrm{obs}}} J_\nu(T(l))\frac{\partial\tau_\nu(l_{\mathrm{obs}},l)}{\partial l}\,\mathrm{d}l, \tag{1}$$

where L_ν is spectral radiance at wavenumber ν at the location of the observer l_{obs}, L_0 is background radiance (assumed zero in this intercomparison experiment), l is the path coordinate, $\tau_\nu(l_1,l_2)$ is the spectral transmittance between two locations l_1 and l_2, and J is the source function, which under conditions of local thermodynamic equilibrium (LTE) depends on kinetic temperature T and frequency, while in non-LTE it depends on state distributions of all involved emitters. The path l, along which the integration is performed, is not a straight line, but, due to wavenumber-dependent

refraction [8], bends towards the Earth. The spectral transmittance $\tau_\nu(l, l-\mathrm{d}l)$ along a path element $\mathrm{d}l$ is calculated according to Beer's law as

$$\tau_\nu(l, l-\mathrm{d}l) = \exp(-\sigma(l, l-\mathrm{d}l)) = \exp\left(-\sum_g \kappa_{g,\nu}(l)\rho_g(l)\,\mathrm{d}l\right), \tag{2}$$

where $\sigma(l, l-\mathrm{d}l)$ is the optical depth of path element $\mathrm{d}l, \kappa_{g,\nu}$ is the absorption cross section of species g at the spectral position ν, which is composed of the contribution of each transition and ρ_g is the number density of species g.

The path l along which Eq. (1) is integrated is determined by the observer position, the viewing angle, and atmospheric refraction. Eq. (1) is either integrated directly by application of a quadrature scheme, or it is solved following the Curtis–Godson [9–12] approach, where layer-related slant path column amounts $u_{g,l}$

$$u_{g,l} = \int_l \rho_g(l)\,\mathrm{d}l \tag{3}$$

and mass-weighted layer mean values p_{CG} and T_{CG} of pressure and temperature

$$p_{\mathrm{CG},g} = \frac{\int_l \rho_g(l)p(l)\,\mathrm{d}l}{u_{g,l}} \tag{4}$$

and

$$T_{\mathrm{CG},g} = \frac{\int_l \rho_g(l)T(l)\,\mathrm{d}l}{u_{g,l}} \tag{5}$$

are used. Each layer l is characterized by its slant path column amounts $u_{g,l}$ and representative state parameters $p_{\mathrm{CG},g}$ and $T_{\mathrm{CG},g}$ which are assumed to be constant within the layers. Use of the Curtis–Godson approach allows relatively long sections of the slant path to be spectrally modelled as an homogeneous path, thus saving on the total number of spectral calculations required.

Resulting spectrally high-resolved radiances (so-called "monochromatic" spectra) are then convolved with the instrument line shape (ILS). The radiance field is convolved with the instrument field of view (FOV). Both these steps are necessary to make simulated spectra comparable to real measurements recorded by a non-ideal spectrometer of finite spectral resolution and finite field of view. In theory, the non-infinitesimal inhomogeneously illuminated field of view of an interferometer leads to a dependence of the ILS from the actual radiance field, which implies that ILS and FOV should be treated in one single step. For practical applications, however, ILS and FOV convolution are often regarded as independent from each other and thus are performed sequentially in an arbitrary order, depending on the architecture of the particular radiative transfer code.

3. The models

Five groups participated in this intercomparison experiment, each with their own line-by-line radiative transfer model: The Karlsruhe Optimized and Precise Radiative transfer code (KOPRA) [13,14] of the Forschungszentrum Karlsruhe, the Reference Forward Model (RFM) of Oxford University (http://www.atm.ox.ac.uk/RFM/), a direct integration radiative transfer code by DLR (MIRART, Modular Infrared Atmospheric Radiative Transfer [15]), the Optimized Forward Model (OFM) by

IFAC (formerly IROE) [16], an enhanced version of the OFM, labelled IROE1, and a radiative transfer code by Rutherford Appleton Laboratory, called FM2D.

3.1. The Karlsruhe optimized and precise radiative transfer algorithm (KOPRA)

The Karlsruhe Optimized and Precise Radiative Transfer Model (KOPRA) is a line-by-line, layer-by-layer model for forward calculation of infrared atmospheric transmittance and radiance spectra for various geometries [13]. Three-dimensional ray tracing for a non-spherical Earth is supported by means of the tangential displacement method [17]. Horizontal inhomogeneities of atmospheric state parameters are linearly approximated by their horizontal gradients. The full three-dimensional treatment of the atmosphere is supported. The hydrostatic constraint can optionally be applied to the input atmospheric data.

The line-by-line calculation of absorption cross sections relies on an optimized implementation [18] of the Humlicek complex error function algorithm [19]. Whenever justified with respect to the user-defined accuracy parameter, pure Doppler or Lorentzian lines are used in order to minimize computational effort. The correction of the theoretical line shapes by the so-called chi-factors [20–22] is supported for CO_2. For this species, line-coupling effects can be considered [23] either by the Rosenkranz approximation [24] or by direct diagonalization, not only for Q-branches but also for P and R branches. Line-coupling effects of other species will be included in a future version. Tabulated pressure and temperature-dependent absorption cross-section spectra of molecules for which no line data are available are interpolated to the actual pressures and temperatures, and resampled in frequency. As an alternative, the so-called pseudolines of these species can be handled in a quasi line-by-line mode, as proposed by G. Toon (private communication). Continua of H_2O, CO_2, N_2, and O_2 are included [25,26]. Furthermore, aerosol continuum emission and extinction can be calculated on the basis of empirical extinction coefficients or on the basis of absorption and extinction cross section as well as phase function spectra generated by a Mie model which is nested with the radiative transfer model. The most recent version also supports a single scattering source function to model the scattering of radiation into the line of sight [27]. KOPRA uses an optimized irregular altitude dependent frequency grid for calculation of absorption cross sections and integration of the radiative transfer equation [28]. Spectroscopic transitions which do not contribute substantially to the overall signal are rejected automatically, where the threshold is driven by a user-defined accuracy parameter. Non-local thermodynamic equilibrium (non-LTE) is taken into account.

The integration of the radiative transfer equation follows a Curtis–Godson approach [9–12]. Since Curtis–Godson mean values are species dependent, while the value of the Planck function is temperature- and wavenumber but not species-dependent, there are several options to calculate the temperature relevant for the source function. Either Curtis–Godson mean values for air, for a certain target species, or an average over the Curtis–Godson mean values of all species, weighted by their individual absorption cross sections can be used. For calculation of the source function in non-LTE applications the latter approach is mandatory.

KOPRA has both internal ILS models and an interface to read pretabulated ILS functions for convolution of the monochromatic spectra and resampling on a user-specified output grid. Furthermore, the numerical radiance integration of the vertical field over an altitude-dependent sensitivity function (field of view function) is supported in the observation angle space rather than tangent altitude space. Here and at other instances KOPRA provides some optimization for calculation of

limb sequences of spectra in a sense that intermediate results which are needed for calculation of spectra of different elevation angles are calculated only once.

3.2. The Reference Forward Model (RFM)

The Reference Forward Model (RFM) is a line-by-line radiative transfer model originally developed from GENLN2 [29] to provide reference spectral calculations for MIPAS. It has subsequently been developed into a general purpose radiative transfer model supporting a wide variety of applications.

The representation of the atmosphere is user-defined but can also be set for automatic sub-layering, where the maximum width of each layer is determined by a limit on the variation in pressure-broadened line width or temperature variation. A two-dimensional option is also available, representing the atmosphere by a series of profiles in the vertical viewing plane with the horizontal coordinate defined by the angle subtended at the Earth centre.

Ray paths through the atmosphere can be defined in terms of elevation angle, geometric or refracted tangent altitudes. The RFM assumes a constant radius of curvature for each path calculation, i.e. a local spherical symmetry. The ray tracing uses different algorithms according to whether a one or two-dimensional atmosphere is used. For one dimension, the FASCODE [30] algorithm is used with altitude as the integrated coordinate and a transformation to avoid the singularity near the tangent point. For two dimensions, a fourth-order Runge–Kutta integration scheme is used to integrate altitude, zenith angle and Earth-centre angle. In both cases, absorber and Curtis–Godson pressures and temperatures are integrated along the ray path. Where segments of different ray paths have similar Curtis–Godson pressures and temperatures the default option is to perform only a single spectral calculation and scale the absorption coefficient by the absorber amount. The refractive index is calculated using a version of Edlen's formula [8].

Spectral calculations can be performed using HITRAN [31] line data, HITRAN cross-section data (tabulated for arbitrary pressure and temperature coordinates), or look-up tables compressed by singular value decomposition (SVD) [32,33] employed for the MIPAS operational processing. For line data, the calculation uses a two-pass system with an initial coarse grid ($0.5\ cm^{-1}$) calculation for the interpolation of line wings up to $25\ cm^{-1}$ from line centre, followed by a fine mesh (typically $0.0005\ cm^{-1}$) for modelling lines within 1–2 cm^{-1} from line centre. Total internal partition sums and molecular cross-section data are those associated with the HITRAN-96 release, although modified for HNO_3. Line shapes are calculated using a modified version of the Humlicek algorithm [34]. For cross-section data a triangulation is used to directly interpolate the associated pressure temperature grid, thus avoiding any intermediate interpolation to resample the pressure and temperature coordinates into a uniform spacing. Both line-coupling and non-LTE are supported by the RFM, and also continua for H_2O, CO_2, O_2 and N_2.

The radiative transfer can either be performed on the fine grid ($0.0005\ cm^{-1}$) or on a user-specified irregular grid. The Curtis–Godson temperature (weighted for each absorber by its absorption) defines the Planck function within each layer but there is also an option to describe the Planck function in terms of a variation with optical depth ("linear-in-tau") [35], which better represents emission from layers of high opacity.

FOV and ILS convolutions are performed internally using externally supplied functions. The FOV convolution is performed in tangent-pointing space, and the ILS convolution in spectral space.

3.3. Modular Infrared Atmospheric Radiative Transfer (MIRART)

The Modular Infrared Atmospheric Radiative Transfer (MIRART) [15] software has been designed for a variety of applications, arbitrary observation geometries, instrumental fields of view (FOV) and line shapes (ILS). Emphasis has been put on efficient and reliable numerical algorithms and a modular approach appropriate for forward simulations and retrieval applications [36].

For the calculation of the Voigt function, MIRART uses an optimized combination of the Humlicek [19] and Hui–Armstrong–Wray [37] complex error function algorithm [38] and switches to pure Lorentzian line shape in the far wings; a further optimization similar in spirit to the work of Kuntz [18] exploits the equidistant wavenumber grid. The wavenumber grid is chosen individually for each altitude level and molecule. Furthermore, a coarse grid is used for contributions of lines outside the spectral region of interest, whereas contributions near the line centre are calculated on a fine spectral grid. Further line shapes supported are Lorentz or Van Vleck–Huber convolved with Doppler.

Line parameters from the HITRAN [31], HiTemp [39], SAO [40], GEISA [41] or JPL [42] spectroscopic data bases can be used in MIRART. The line strength conversion from the reference temperature used in the database to the atmospheric temperature follows the scheme used in the ATMOS software [43].

In addition to the line contributions, continua are implemented for water (Clough–Kneizys–Davis (CKD) continuum, Version 2.2), carbon dioxide, oxygen, and nitrogen [25,26]. Alternatively the Liebe dry air continuum [44] or an empirical continuum for the far infrared provided by K. Chance (private comm., 1996) can be used.

The solution of the radiative transfer equation (1) and Beer's law (2) requires the integration of spatially varying quantities, which are given only for a set of discrete altitude points along the line of sight. These integrals are—in contrast to the Curtis–Godson approach—calculated using standard numerical quadrature schemes. Thus, in contrast to the other codes discussed here, absorption cross sections, absorption coefficients, etc. are calculated for pressure $p(z_n)$ and temperature $T(z_n)$ at altitude levels z_n rather than for $p_{\mathrm{CG},g}$ and $T_{\mathrm{CG},g}$ of layers $[z_n, z_{n+1}]$. Path-dependent quantities entering Eqs. (1) and (2) are obtained from altitude-dependent quantities by simple geometric mapping from z to l. MIRART has implemented a trapezoid quadrature scheme, the method of overlapping parabolas, and a piecewise cubic Hermite quadrature [45]. These quadrature rules work for arbitrarily spaced (i.e. not necessarily equidistant) abscissas.

MIRART offers the choice of field-of-view convolution either in the tangent altitude space or in the elevation angle space using Gaussian quadrature rules appropriate for the chosen sensitivity function.

3.4. The Optimized Forward Model (OFM)

The Optimized Forward Model has been developed for application in the operational near-real-time processing of MIPAS spectra [16]. This implies that major effort has been spent for minimization of computational requirements. In particular, the sequence of operations has been organized so that unnecessary repeated calculations are avoided and the available random access memory of the computer is fully exploited.

In a first step, the line of sight is determined taking into account the refraction and assuming a locally spherical Earth shape.

The atmosphere is then layered assuming horizontal homogeneity. The boundaries of the layers are automatically set such that the variation across the layers of both temperature and the Voigt half-widths of a reference line are below pre-defined thresholds. For each layer, Curtis–Godson representative pressure and temperature are determined. Curtis–Godson quantities are calculated explicitly only for all path segments related to the lowest limb view and the tangent layers of the other limb views, while they are derived by the secant law approximation for the other path segments. This is a very effective optimization as it dramatically reduces the number of different pressure/temperature pairs for which cross sections are to be calculated.

The absorption cross sections can either be calculated line by line, using a pre-selected spectroscopic database and fast Voigt profile computation [46], or be read from pre-computed look-up tables [33], which were generated by means of the RFM. Since the consistency of the two approaches was demonstrated during the implementation phase [16], in this study only the LBL mode of the OFM was assessed. In the line-by-line calculation of the cross sections, line-mixing, pressure-shift, self-broadening, and non-local thermodynamic equilibrium (NLTE) are neglected.

Finally, the radiative transfer integral is computed as a summation of the contributions of a set of discrete layers. In this computation the symmetry of the line-of-sight about the tangent point is exploited. The radiative transfer is computed for a minimal and optimized set of frequencies (irregular grid) allowing a satisfactory reconstruction (by interpolation) of the full high-resolution atmospheric spectrum that is usually represented on a fine (typically $0.0005\ \mathrm{cm}^{-1}$) frequency grid. The reconstruction of the full high-resolution spectrum and the convolution by the instrument line shape are done in a single optimized step to save computing time. The ILS function is an input of the program and can be optionally apodized [47].

Using the above procedure, AILS convolved spectra are simulated for a set of tangent altitudes that includes the tangent altitudes of the measured spectra and some additional altitudes necessary for an accurate FOV convolution. The spread of the FOV in the altitude domain is constructed with linear interpolation from a tabulated function. The FOV pattern is assumed to be constant with the scan angle. The effect of field of view is then taken into account by performing, for each spectral frequency, the convolution between the tangent altitude-dependent spectrum and the FOV pattern. The variability of the spectrum as a function of tangent altitude is determined by interpolating a polynomial through the spectra simulated at contiguous tangent altitudes in the range of the FOV pattern.

3.5. The Extended IROE Model (IROE1)

The Extended IROE Model (IROE1) is based on the OFM but includes several improvements. Pressure-shift, and self-broadening have been included in the model, while local thermodynamic equilibrium is still assumed. Furthermore, an additional option was implemented in the IROE1 model allowing the inclusion of HITRAN pre-tabulated absorption cross sections of heavy molecules. Line-mixing has been included in a later version. Thus, the line-mixing option of the IROE1 code has not been assessed in this study.

3.6. The Two-Dimensional Forward Model (FM2D)

The RAL forward model, FM2D, is a line-by-line code that allows modelling of the atmosphere in two dimensions with the field expressed as a two-dimensional, vertical and horizontal section.

Operation in a one-dimensional mode, where the atmosphere is assumed to be spherically symmetric and so may be represented by a single vertical profile, is also possible. Originally, designed for microwave wavelengths [48], it has been extended in scope, particularly by inclusion of appropriate continuum formulations, such as that by Clough et al. [25], to allow mid-infrared radiative transfer calculations to be carried out. The model allows application of an instrument function, in terms of basic parameters such as spectral response and field of view, and performs direct, analytic calculation of "weighting functions" (rows of the Jacobian matrix of the forward model radiances with respect to retrieval parameters) for atmospheric parameters.

FM2D has two main parts, an initialization module and a radiative transfer module. The former deals with the all input parameters including atmospheric model definition, line shape and spectral grid selection, and instrument characteristics, such as spectral response and field of view. To carry the radiative transfer quadrature, a set of computational grid points in the horizontal and vertical are defined. The module calculates the weights for the interpolation from the points at which atmospheric fields are specified to the computational grid, and also determines the basis functions for the derivatives of the field on the computational grid with respect to perturbation at the points at which input data is specified. This approach allows rapid repeated determination of line-of-sight integrals and weighting functions.

The radiative transfer module calculates radiances and their derivatives with respect to the atmospheric state for the required number of pencil-beam views. The ray-tracing scheme includes refraction which may be modelled in a rigorous two-dimensional manner or, alternatively, by assuming horizontal symmetry about the geometric tangent point, which makes the calculation much more rapid and is adequate for many scenarios. The calculation of absorption coefficients follows from evaluation of spectral line and continua contributions; the Voigt line shape calculation used is the Wells [34] version of the modified Humlicek algorithm, which also is used by the RFM. Therefore, any pure LBL calculation with Voigt line shapes for a homogeneous path with these two models ought to agree.

To restrict computational memory requirements, monochromatic spectra are convolved with spectrometer response functions for each view, and only the convolved radiances and weighting functions are stored. Once these spectrometer-convolved values have been computed for all pencil-beams, they are convolved with the instrument field of view function before being output.

4. The intercomparison experiment

In order to detect forward model deficiencies, a cross comparison exercise was carried out to mutually validate radiative transfer codes. The idea of the setup of the intercomparison exercise was to start from simple settings proving the basic functionalities of the radiative transfer codes, and then to proceed to more complex and realistic scenarios. In order to avoid any masking of differences in the basic functionalities of the codes by additional sophistication introduced by realistic atmospheric simulations, the first set of tests refers to cell transmittance calculations (Table 1). In a second step, atmospheric limb emission spectra have been intercompared (Table 2). The profiles of atmospheric state parameters used are shown in Figs. 1 and 2. Unless explicitly mentioned, the HITRAN-98 spectroscopic database, which is an update of Ref. [31], was used. For CFC-12, cross-section data measured by Varanasi [49] and subsequent updates were used. Furthermore,

Table 1
Cell transmittance test cases

Test Id.	Spectral region (cm^{-1})	Cell length (m)	Species	VMR (ppmv)	p (hPa)	T (K)	Continua	Chi factor	Line mixing	ILS
1	1270.0–1280.0	5.0	N_2O[a]	100	1013.25	296	—	—	—	—
2	1274.2–1275.0	5.0	N_2O[a]	100	20.0	296	—	—	—	—
3	1274.2–1275.0	20	N_2O[a]	100	2.0	296	—	—	—	—
4	1274.2–1275.0	20	N_2O[a]	100	2.0	296	—	—	—	Yes[b]
5	1274.2–1275.0	20	N_2O[a]	100	2.0	296	—	—	—	Yes[c]
6	1274.2–1275.0	20	N_2O[a]	100	2.0	296	—	—	—	Yes[d]
7	1270.0–1280.0	5	N_2O[a]	100	1013.25	250	—	—	—	—
8	1274.2–1275.0	5	N_2O[a]	100	20.0	250	—	—	—	—
9	1274.2–1275.0	20	N_2O[a]	100	2.0	250	—	—	—	—
10	1830.0–1840.0	50.0	NO	5×10^2	20.0	250	—	—	—	—
			N_2O	5×10^5						
			O_3	1×10^5						
11	2390.0–2500.0	10^6	CO_2	355	250	296	—	Yes	—	—
12	2390.0–2500.0	10^6	CO_2	355	250	250	—	Yes	—	—
13	715.0–725.0	50.0	CO_2	355	250	250	—	Yes[e]	Yes	—
14	715.0–725.0	50.0	CO_2	355	50	250	—	Yes[e]	Yes	—
15	738.0–744.0	500.0	CO_2	355	250	250	—	Yes[e]	Yes	—
16	738.0–744.0	1000.0	CO_2	355	50	250	—	Yes[e]	Yes	—
17	1600.0–1610.0	100.0	H_2O	1000	250	250	Yes	—	—	—

[a]Only one transition at 1274.6166 cm^{-1} to be considered.
[b]Unapodized instrument line shape.
[c]Apodized instrument line shape.
[d]Apodized simplified (pretabulated) instrument line shape.
[e]Chi-factor may not be active in this microwindow under consideration of line mixing.

vibrational temperatures [50], pretabulated MIPAS-FOV and AILS were provided to the participants to be used where appropriate.

4.1. Line intensities and evaluation of spectral line shape

First, the calculation of line intensities and the evaluation of spectral line shapes have been assessed for various pressures and temperatures. Three different pressures were chosen, corresponding to dominating pressure broadening, to dominating Doppler broadening, and to balanced pressure and Doppler broadening, respectively. Calculations were carried out for the HITRAN reference temperature of 296 K as well as for 250 K which is more realistic for stratospheric conditions. In order to better detect differences between the modelling approaches, single transition monochromatic transmittance spectra have been intercompared, i.e. spectra which have not been convolved by any instrument line shape function (tests 1–3 and 7–9).

In test 2, which serves as an example for illustration, and throughout all cell transmittance calculations, the RFM and FM2D results agree extraordinarily well (Fig. 3). This is explained by the

Table 2
Atmospheric radiance test cases

Test Id.	Spectral region (cm^{-1})	Tangent altitude (km)	Species considered	FOV	ILS	Continua	Line mixing	Non LTE
18[a]	1215.0–1217.0	15	H_2O, CO_2, O_3 N_2O, CH_4	—	—	Yes	—	—
19[b]	1215.0–1217.0	15	H_2O, CO_2, O_3 N_2O, CH_4	—	—	Yes	—	—
20	1215.0–1217.0	40	H_2O, CO_2, O_3 N_2O, CH_4	Yes	Yes	Yes	—	—
21	1215.0–1217.0	15	H_2O, CO_2, O_3 N_2O, CH_4	Yes	Yes	Yes	—	—
22	790.0–794.0	15	CO_2, O_3	—	—	—	Yes	—
23	790.0–794.0	15	CO_2, O_3	Yes	Yes	—	Yes	—
24	920.0–940.0	15	CO_2, O_3, CFC-12	—	—	—	Yes	—
25	920.0–940.0	15	CO_2, O_3, CFC-12	Yes	Yes	—	Yes	—
26	1600.0–1610.0	10	H_2O, N_2O, CH_4 O_2, NO_2	Yes	Yes	Yes	—	—
27	675.5–676.5	100	CO_2, O_3	Yes	Yes	Yes	—	—
28	675.5–676.5	100	CO_2, O_3	Yes	Yes	Yes	—	Yes
29	967.0–968.0	100	CO_2, O_3	Yes	Yes	Yes	—	—
30	967.0–968.0	100	CO_2, O_3	Yes	Yes	Yes	—	Yes

[a]Standardized altitude grid of 1 km used for integration of radiative transfer equation.
[b]Default altitude grid used for integration of radiative transfer equation.

fact that both FM2D and RFM use the same modified Humlicek algorithm by Wells [34]. The KOPRA relies on a Humlicek implementation by Kuntz [18]; differences between the original Humlicek and the Kuntz implementation are below 2×10^{-6}; RFM-KOPRA FM2D-KOPRA differences are explained by the use of different Humlicek implementations, which switch between accuracy-driving Humlicek regions at slightly different distances from the line centre. However, since these differences are very small, they are not of significance.

The OFM uses the original Humlicek algorithm [19] but switches to pure Lorentzian line shape quite close to the line centre; the major part of differences is attributed to the fact that the OFM calculates the Voigt function only in some spectral grid points and uses linear interpolation in between.

MIRART uses yet another Voigt implementation, utilizing the Hui et al. approach [37] near the line centre, Lorentzian line shape in the far wings, and Humlicek [19] in between. The structure in the difference plot is explained by the fact that for this case MIRART calculates only three data points by means of Humlicek region 1, and switches to Lorentzian shape quite soon. By application of the Voigt instead of Lorentzian line shape within a wider spectral interval around the line center, this discrepancy could be removed. The accuracy of the Humlicek 1982 algorithm is about 10^{-4}, the accuracy of the Hui algorithm is about 10^{-5} to 10^{-6}. Thus, the use of different Voigt algorithms can explain the observed differences, i.e., all differences are in the order of size or smaller than the accuracy specification of the original Humlicek algorithm.

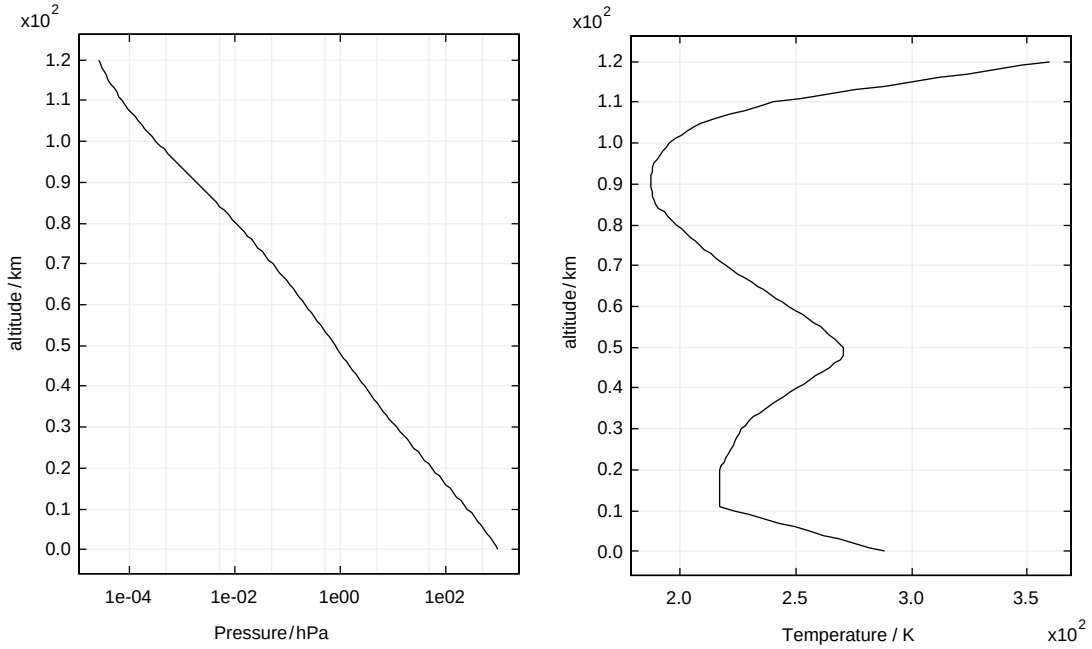

Fig. 1. Pressure and temperature profiles used for test cases 18–30.

Comparison of spectra calculated for 296 K and those calculated for 250 K gives no hint of any particular problem with temperature dependence of line intensities, except for MIRART, which reveals a factor of two larger differences than for the 296 K case. There seems to be a component in the differences which is caused by the temperature-dependent line intensity. MIRART uses the scheme as proposed by Norton and Rinsland [43], while all the other codes use the Gamache [31] total internal partition sum parametrization.

In summary, it can be concluded from test cases 1–3 and 7–9 that the calculation of line strengths and the evaluation of the line shapes is performed by each code within the individual accuracy specification.

4.2. Instrument line shape

In a next step, monochromatic spectra were convolved by an instrument line shape (Tests 4–6). While some codes include tools to provide instrument line shapes for dedicated instrument specifications (e.g. KOPRA [51]), this intercomparison focuses on the case of a pretabulated instrument line shape (Test 6), which was an "ideal" Fourier transform spectrometer line shape related to 20 cm optical path difference plus Norton–Beer "strong" apodization [47]. All the differences in the calculated spectra are very small (below 0.2%) and probably not significant for real data analysis. A small offset of -0.4×10^{-6} between the RFM and KOPRA is attributed to renormalization of the ILS by the RFM. Much of the structure in the RFM–KOPRA difference is simply due to the numerical precision of the output, and disappears when the RFM output is written with double precision. In summary, there is no evidence of any substantial ILS-convolution problem in any of the codes.

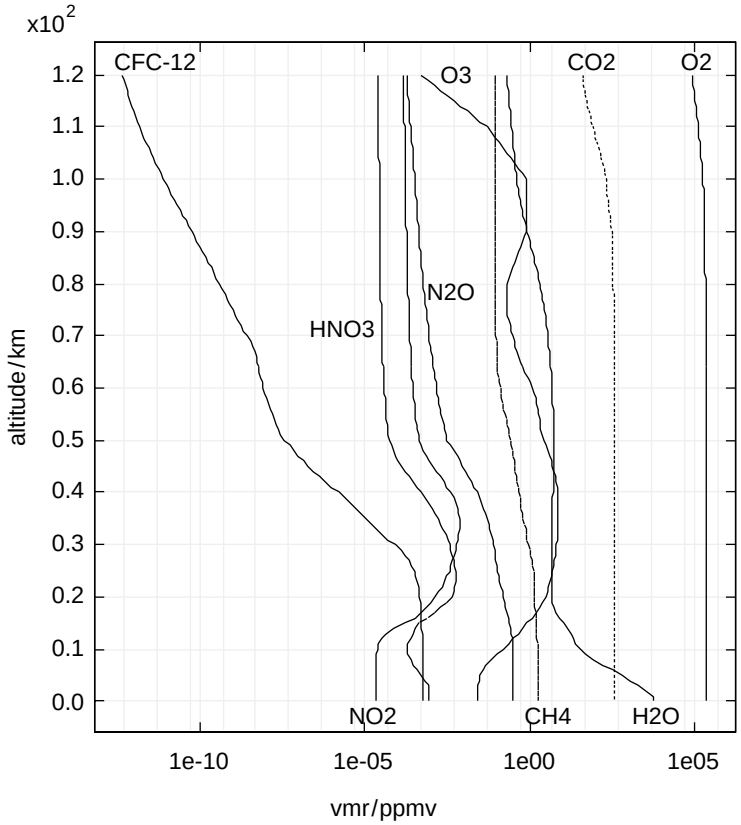

Fig. 2. Vertical profiles of volume mixing ratios of trace species used for test cases 18–30.

4.3. Line rejection criteria

In theory every transition contributes to the signal at every frequency grid point. Since consideration of all transitions obviously is not practicable, each model applies a line wing truncation or line rejection criterion, which is driven by the optimal trade-off between computational efficiency and accuracy. Different choice or implementation of such criteria leads to remarkably different results in test cases 10 and 11.

In test case 10 (Fig. 4), both RFM and FM2D difference spectra reveal smaller continuum-type background extinctions than KOPRA spectra. RFM and FM2D use a$\pm$25 cm^{-1} line rejection criterion around each 1 cm^{-1} sub-interval; KOPRA, OFM, and IROE1 use a$\pm$25 cm^{-1} line rejection criterium around the microwindow boundaries, i.e. use more transitions outside the microwindow, which explains larger background absorption. MIRART uses a$\pm$10 cm^{-1} line rejection criterion around the microwindow boundaries by default, except for H_2O-lines, where this value is set to 25 cm^{-1} in order to comply with the water vapour continuum implementation. Although it might be expected that the various truncation limits would lead to continuum-like difference spectra, the non-linearity of radiative transfer means that the difference spectra also exhibit some line structure.

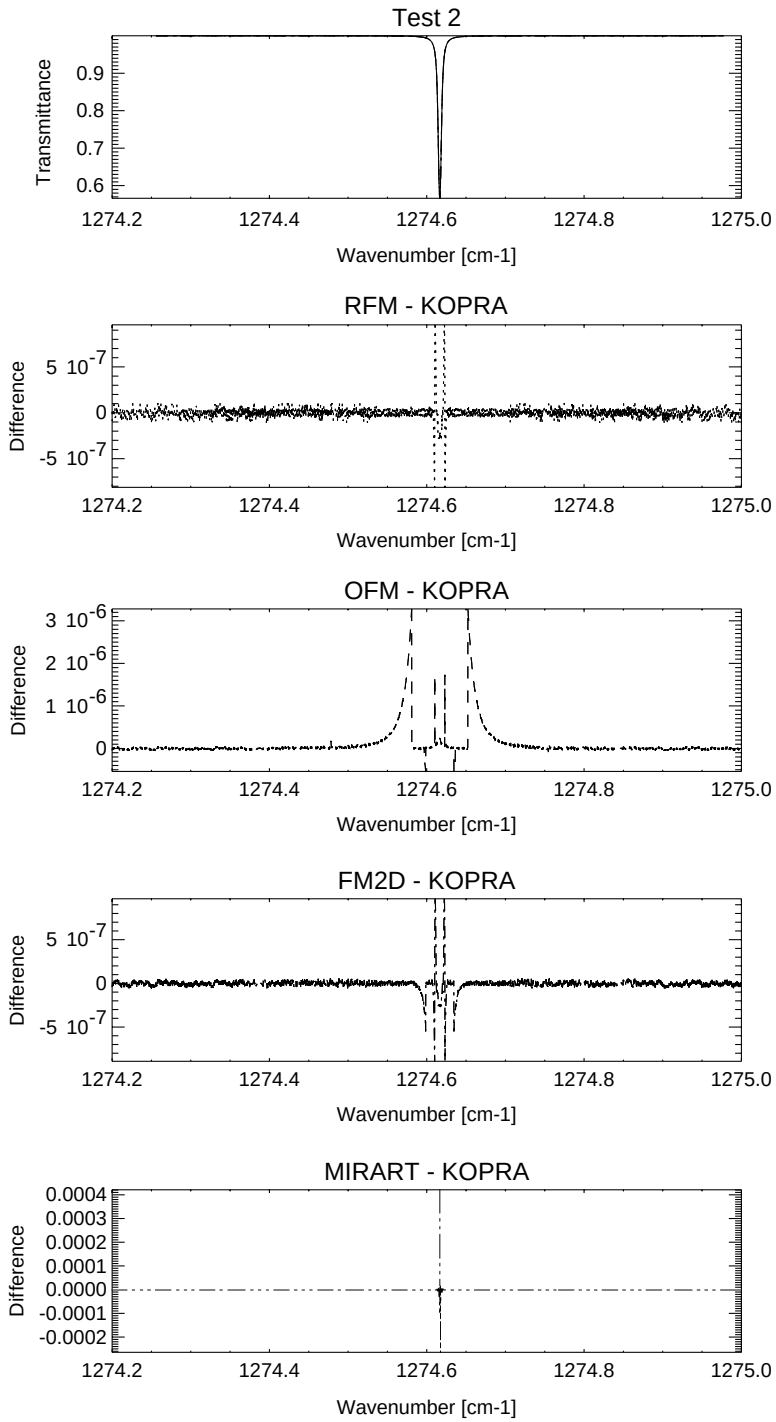

Fig. 3. Single line transmission spectra (test case 2). The uppermost panel shows the spectra, whereas the other panels show difference spectra with respect to KOPRA. Differences between the spectra are so small that they are not resolved in the uppermost panel, which indeed includes all five spectra under investigation.

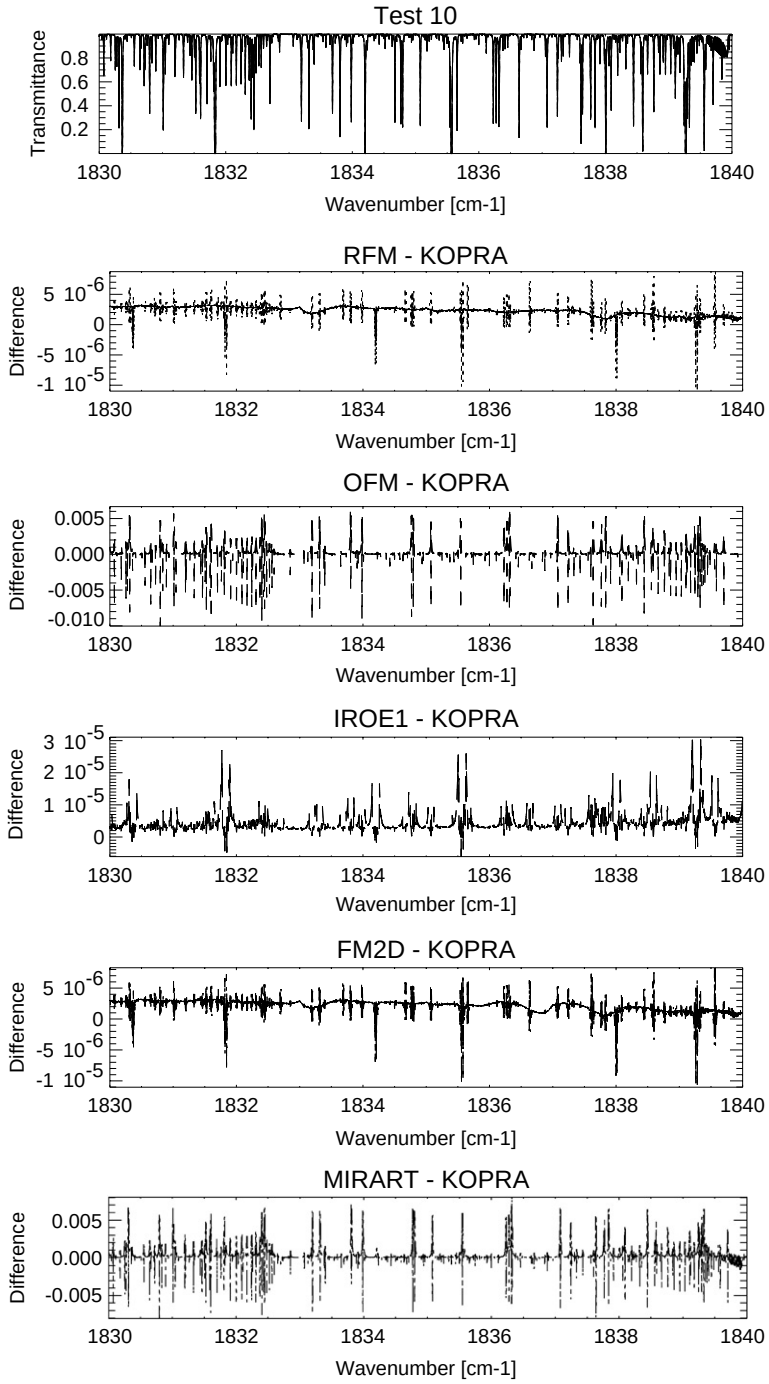

Fig. 4. Multi-transition transmittance spectra (test case 10). The uppermost panel contains the spectra, whereas the other panels show difference spectra with respect to KOPRA. Differences between spectra are so small that they are not resolved in the uppermost panel.

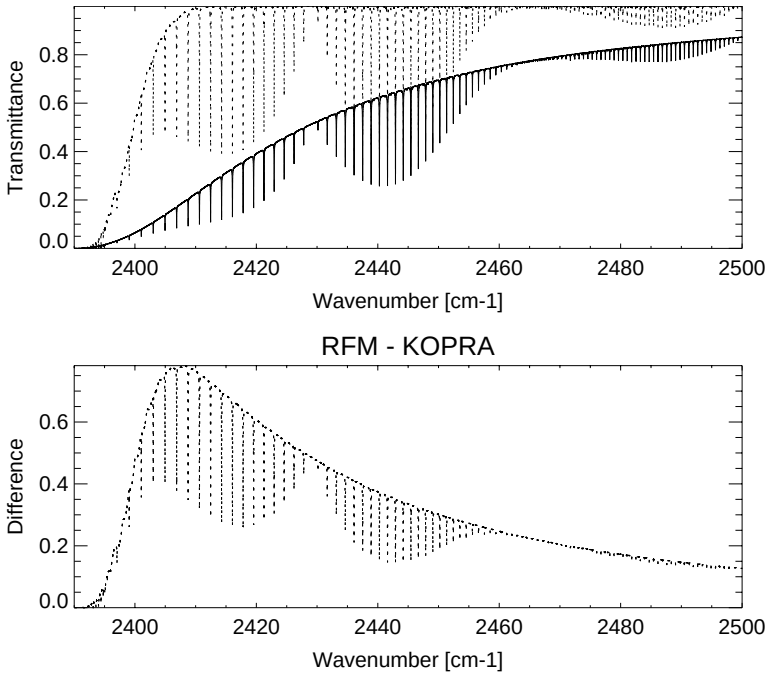

Fig. 5. Transmittance difference between RFM (dotted line) and KOPRA (solid line) in the 4.3 μm-region. Differences are attributed to different line rejection criteria. The test scenario is as for test case 11 except that no chi-factor has been applied.

A prominent example, which shows what impact different line rejection criteria can have on spectral calculations, is the 4.3-μm region of CO_2 (Fig. 5). While these spectra have not been calculated as a test case in themselves but as a reference for test case 11 (without application of the chi-factors discussed in Section 4.5), the dramatic effect of different line rejection criteria between KOPRA and RFM is clearly evident. These differences disappear when RFM considers a pretabulated CO_2-continuum that accounts for the otherwise neglected extreme line wings.

4.4. Self broadening

Large OFM–KOPRA and MIRART–KOPRA differences in test case 10 (Fig. 4) are explained by the fact that neither the OFM code nor MIRART consider self-broadened half-widths; the half-widths of all the lines are calculated using only the air-broadened half-width parameter. This approximation should not turn out to be too coarse in real atmospheres, but makes a substantial difference in high-resolution cell transmittance calculations.

In contrast, the IROE1 code includes the "correct" calculation of self-broadening, and its results agree much better with the other codes than the OFM code does. The residual difference is caused by interpolation effects as explained under test cases 1–3. These effects add up in case of multi-transition calculations.

4.5. Chi-factor implementation

The impact of time dependence of collisions on the line shape is usually considered by empirical correction functions, the so-called chi-factors, which account for the observed sub-Lorentzian behaviour. All chi-factor implementations under assessment in this study rely on Refs. [20–22]. In test case 11 the chi-factor implementation is analysed for the 4.3 μm CO_2 band at 296 K (Fig. 6). Large differences between KOPRA and RFM spectra are caused by different line rejection criteria rather than different chi-factor implementation (cf. Section 4.3 and Fig. 5). OFM uses the same line rejection criteria as KOPRA; thus the differences are significantly smaller. There is some continuum-type difference which could be related to a chi-factor related issue. These differences, however, are less than a tenth of a percent of the chi-factor effect itself. FM2D does not include any chi-factors, which explains the difference and reveals the importance of the chi-factor in this wavenumber region.

Assessment of test case 12, which is identical to case 11 except that the temperature is 250 K, gives no evidence of any problems related to the temperature dependence of the chi-factor.

In summary, there is no evidence of major chi-factor related problems in any of the models. The large spectral differences found could be attributed to different line rejection criteria.

4.6. Line coupling

The line coupling characteristics of the forward model was assessed for Σ–Π- and for Π–Δ-type bands. Tests 13 and 14 assess the Σ–Π CO_2 Q-branch near 720 cm^{-1}, whereas tests 15 and 16 cover the Π–Δ-type CO_2 Q-branch near 741 cm^{-1}. Test cases 22 and 23 are the related atmospheric limb emission scenarios. The RFM uses the Rosenkranz approximation [24] as described in Ref. [52], while KOPRA supports the direct diagonalization approach, which is considered more accurate in particular for high pressures. Fig. 7 shows the results of test case 13, which is the 720 cm^{-1} Q-branch at 250 hPa. Comparison of net effects of line mixing in RFM and KOPRA spectra proves that the different treatment of line mixing is fully responsible for the differences between RFM and KOPRA spectra. Furthermore, by selecting the Rosenkranz approximation in KOPRA, the differences disappeared. At 50 hPa, the differences between RFM and KOPRA are a factor of 100 smaller than for the high-pressure test case 13. This is due to the fact that the KOPRA code switches automatically to the Rosenkranz approximation for lower pressures, since this algorithm then approximates the line coupling effect quite accurately. If the KOPRA code is forced to apply direct diagonalization also for low pressures, differences increase by a factor of three.

The OFM and FM2D codes do not consider line mixing at all. This explains the differences and shows the significance of line mixing for the given conditions. As expected, residuals are much lower (a factor of six) in the low-pressure case than in the high-pressure one.

The same explanations apply to test cases 15 and 16 (Π–Δ-type CO_2 Q-branch at 250 and 50 hPa, respectively). Application of the codes to atmospheric conditions (test case 22, 792 cm^{-1} CO_2 Q-branch) leads to deviations between RFM and KOPRA spectra of 0.6% at the band head, while the net effect of line mixing is 10%. Test case 23, which is identical to case 22 except that the MIPAS instrument line shape as well as the field of view are considered, proves that the effect of line mixing clearly exceeds the MIPAS noise level (up to a factor of 10). Compared to test case 22, the differences between KOPRA and RFM are increased and are now in the order of size of the noise level. The dominating reasons for these discrepancies, however, are not the different line

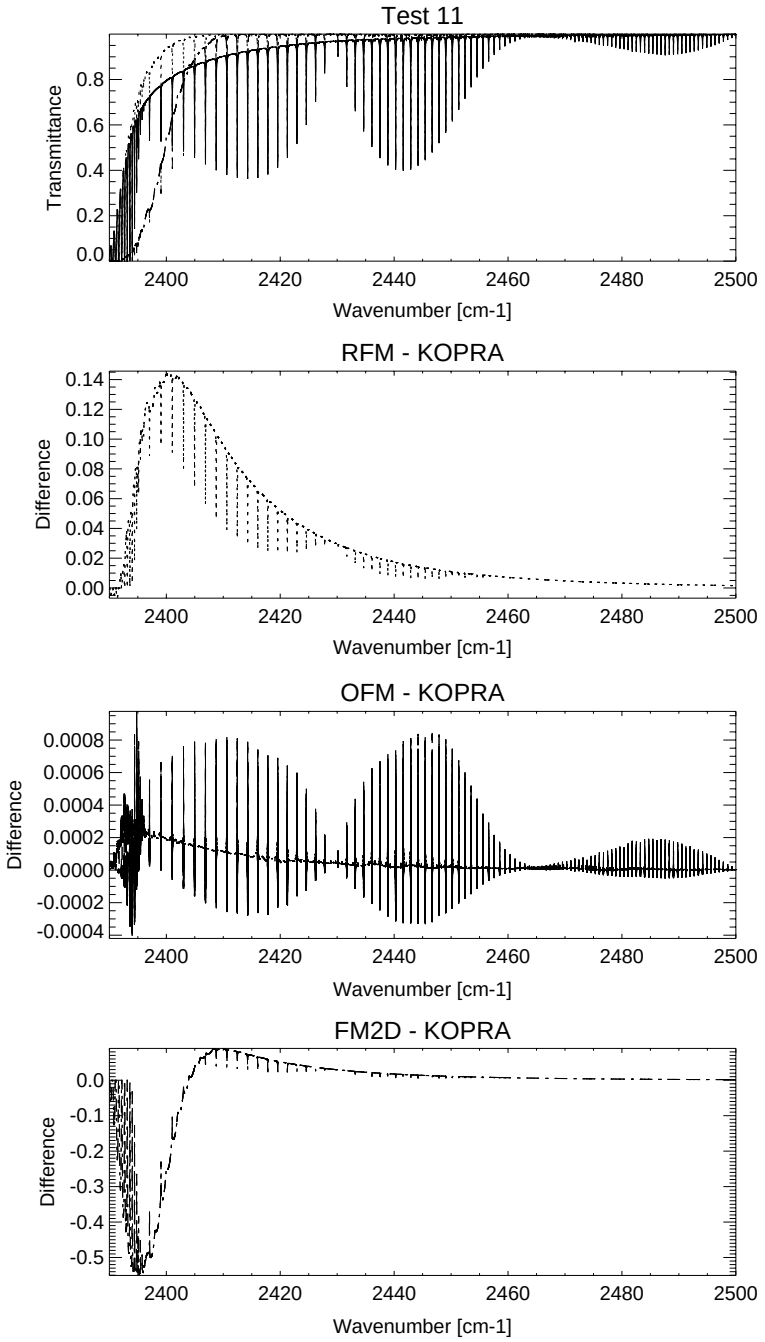

Fig. 6. Chi-factor (test case 11). The uppermost panel shows the transmittance spectra, whereas the other panels show difference spectra with respect to KOPRA.

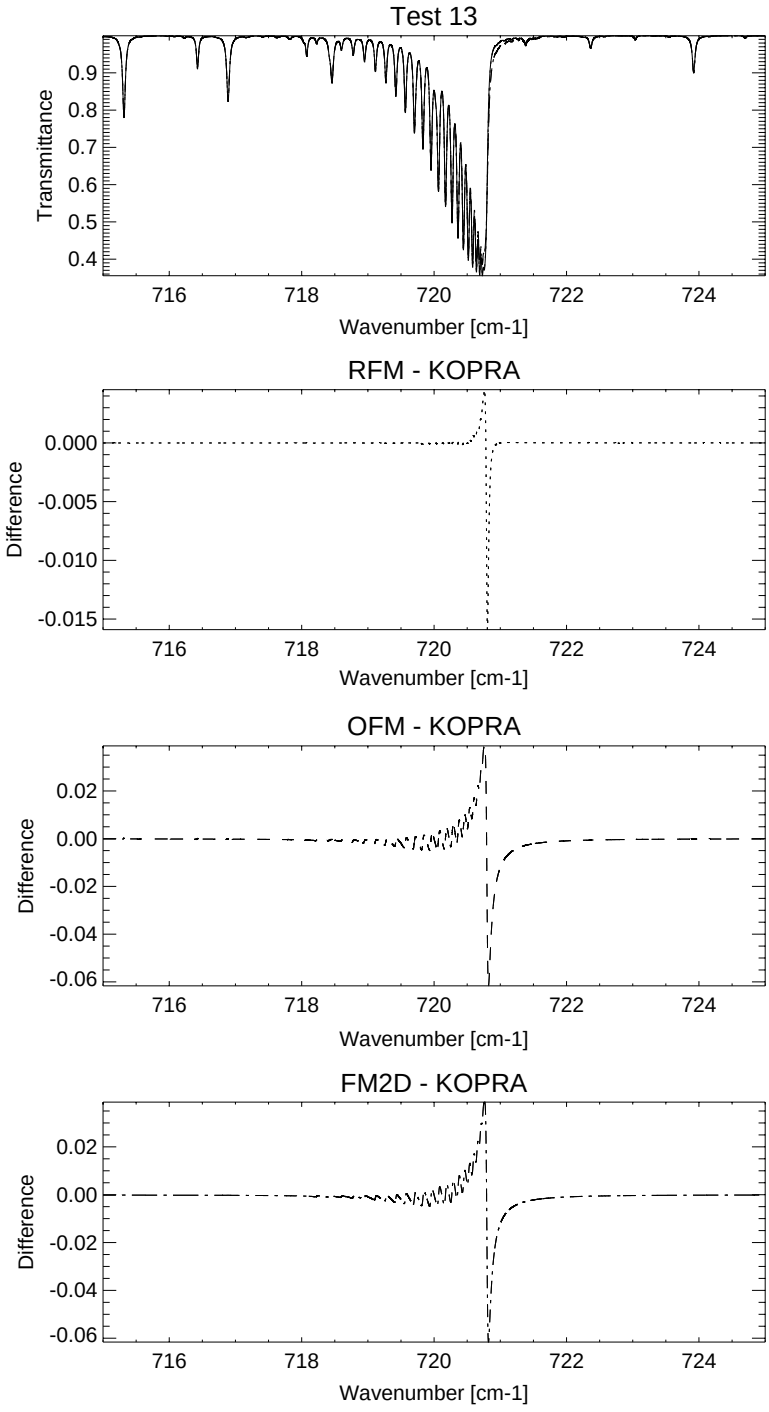

Fig. 7. *Q*-branch line coupling (test case 13). The uppermost panel shows the transmittance spectra, whereas the other panels show difference spectra with respect to KOPRA. Differences between spectra are so small that they are hardly resolved in the uppermost panel.

mixing implementations, but the different line wing cut-off criteria, as well as different numerical treatments of the integration of the radiance field over the non-infinitesimal instrument field of view. Even for these test cases for realistic conditions the neglect of line coupling in FM2D and OFM remains the driving source of the differences when compared to KOPRA or RFM. These differences exceed the MIPAS noise level by far and reach 350–400 $nW/(cm^2\,sr\,cm^{-1})$.

Another phenomenon of collision-induced perturbation of energy levels is pressure shift, which was found to be important, too. This feature is included in all codes except OFM. No pressure shift-related residuals were found in the spectra which have been calculated under consideration of pressure shift, except for atmospheric calculations where different treatment of atmospheric refraction in one of the codes caused different effective pressure (test case 18).

4.7. Water vapour continuum

Test cases 17 and 26, where the water vapour continuum was assessed, have been intentionally chosen to be identical to the "Intercomparison of Transmittance and Radiance Algorithms" (ITRA) in the late 1980s [4], in order to allow further comparison. RFM and FM2D spectra agree extraordinarily well (Fig. 8); this is attributed to the fact that the basic theory and methodology for modelling far line wings/continuum are the same in both these codes. While the practical implementation and coding are different, both codes use the Wells' version of the Voigt routine [34].

The different line rejection criterion (cf. test case 10) does not hold here as an explanation for differences between RFM–KOPRA and FM2D–KOPRA, because in the case of activated continua-parametrizations, KOPRA also uses the grid point related rejection criterion at 25 cm^{-1} in order to be consistent with the continuum specification. The following versions of CKD continua have been used: KOPRA: CKD 2.4; RFM: CKD 2.1; MIRART: CKD 2.2; OFM: CKD 2.1.; FM2D: CKD 2.1. The use of the CKD 2.4 water vapour continuum in the IROE1 code results in improved consistency with the other codes. The remaining discrepancies are attributed to line shape effects as discussed in test cases 1 and 2.

Compared to the ITRA exercise, where dramatic differences in calculated radiance spectra were caused by different—or missing—water vapour continuum implementations there is excellent agreement between all codes now.

4.8. Treatment of inhomogeneous atmosphere

While the overall agreement of radiance spectra calculated typically was good, the numerical treatment of the inhomogeneous atmosphere proved to deserve major attention (test cases 18–21). The choice of the altitude grid on which the integration of the radiative transfer equation is performed, as well as the interpolation rule of volume mixing ratios with altitude (linear versus logarithmic) has a visible impact on the radiance spectra which can cause differences of about 2% in some cases. There was no evidence for spectral differences due to different modelling of atmospheric refraction, except for MIRART which did not consider refraction in its version used for this intercomparison experiment. Even at 15 km tangent height, however, the difference is negligible, since in this test the geometry has been specified in terms of tangent height rather than elevation angle.

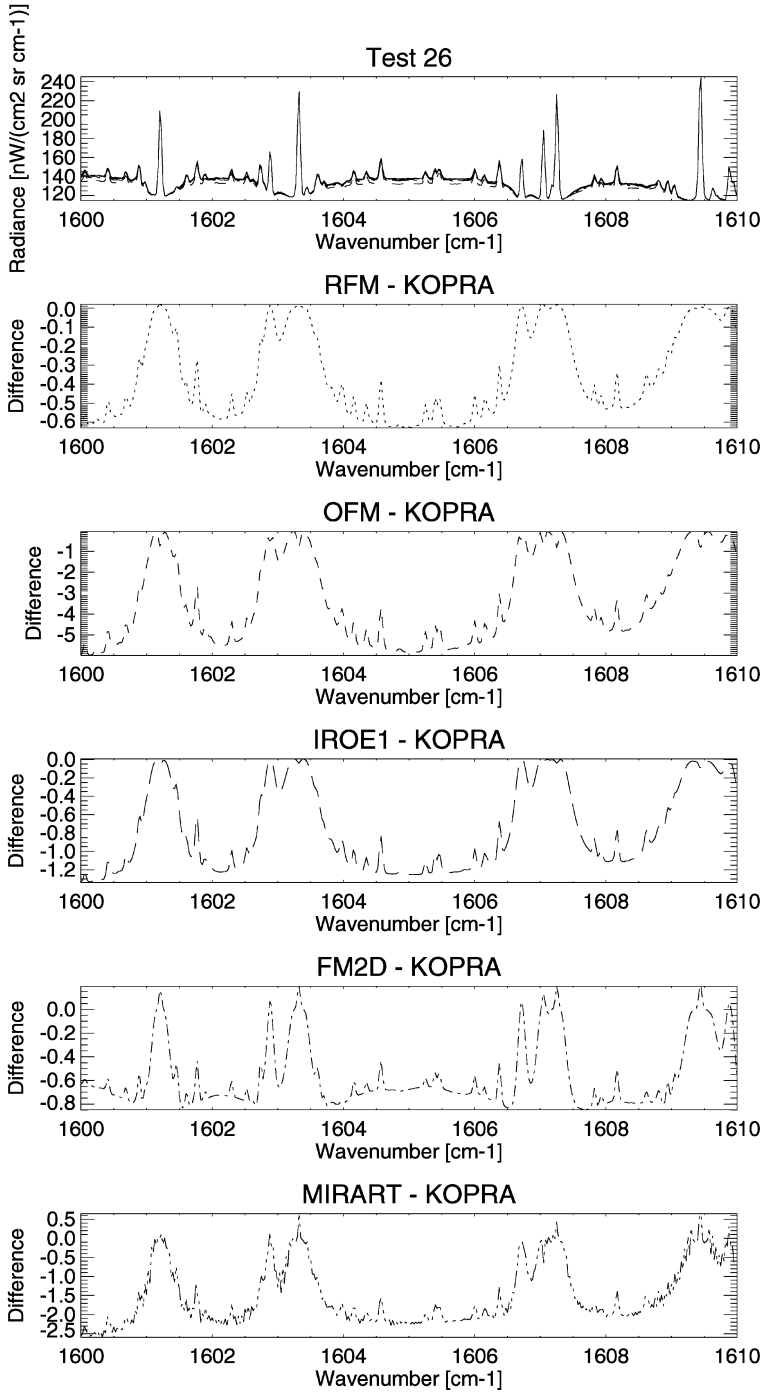

Fig. 8. Water vapour continuum (test case 26). The uppermost panel are radiance spectra (KOPRA: solid; RFM: dotted; OFM: dashed; IROE1: long dash; FM2D: dashed–dotted (overlaid with RFM); MIRART: dashed doubledotted). The other panels show difference spectra with respect to KOPRA.

4.9. Field of view convolution

The numerical integration of the calculated radiance over the non-infinitesimal field of view of the MIPAS instrument is handled in a different manner in the codes under investigation. Differences refer to both the number of pencil beams used for the numerical integration as well as to the interpolation rules applied to the values of the field of view function and the radiance field.

KOPRA and RFM spectra agree well, both in magnitude and shape (Fig. 9); also the shape of residual patterns with OFM and FM2D agree well. The number of pencil beams used for convolution of the radiance field with the field of view function is of particular importance. KOPRA uses 17, which may be too many for quasi-operational use. RFM uses 14 points. FM2D uses 10 pencil beams, while the OFM uses 3 pencil beams only; this should explain the observed differences. MIRART used 12 pencil beams selected at specific tangent heights to avoid interpolation of the pencil beam radiances in the tangent altitude.

Some differences are explained by the fact that the FM2D assumes linear variation with elevation in the product field-of-view response times pencil beam radiance, while RFM assumes linear variation in both these quantities, and thus quadratic variation of the product. As expected, these differences become smaller, when more pencil beams are used in FM2D. The OFM assumes linear variation of the field-of-view function, while the pencil beam radiance variation with altitude is described by a polynomial of degree equal to the number of pencil beams minus one.

All difference spectra are correlated/anticorrelated to the radiance spectrum; this first suggests that differences resulting from different weighting of the pencil beams in their numerical convolution with the field of view would be responsible for the differences. This, however, could be ruled out for the comparison with RFM spectra by comparing infinitesimal field-of-view spectra (pencil beam calculations): These differences are of the same order of magnitude as the field of view convolved spectra differences. Instead, the differences in field of view convolved spectra are attributed to the different continuum levels.

For OFM and FM2D spectra without field of view the differences are reduced by a factor of 3 and 4, respectively. That means that the largest part of the differences in the test with field of view is due to field of view convolution.

A particular problem with the tabulated field of view used here should be mentioned in conclusion: The ESA-supplied functions are not always tabulated down to zero response, since the field-of-view measurements distributed by ESA did not always cover the entire field of view. Different codes handle this problem in a different manner. The FM2D code sharply cuts off the field-of-view function to zero after the last tabulated data point. The RFM sets zero points one field-of-view grid point space away from the last point. Also the OFM extrapolates the field of view sensitivity smoothly down to zero. Meanwhile the MIPAS field-of-view as measured has been attributed to a non-appropriate measurement setup and thus has been withdrawn.

4.10. Absorption cross sections of heavy molecules

The spectral features of heavy molecules are not calculated in a line-by-line mode but by interpolation of cross section spectra measured at different pressures and temperatures. In test cases 24 and 25 the CFC-12 band system near 920 cm^{-1} has been chosen to assess the cross-section

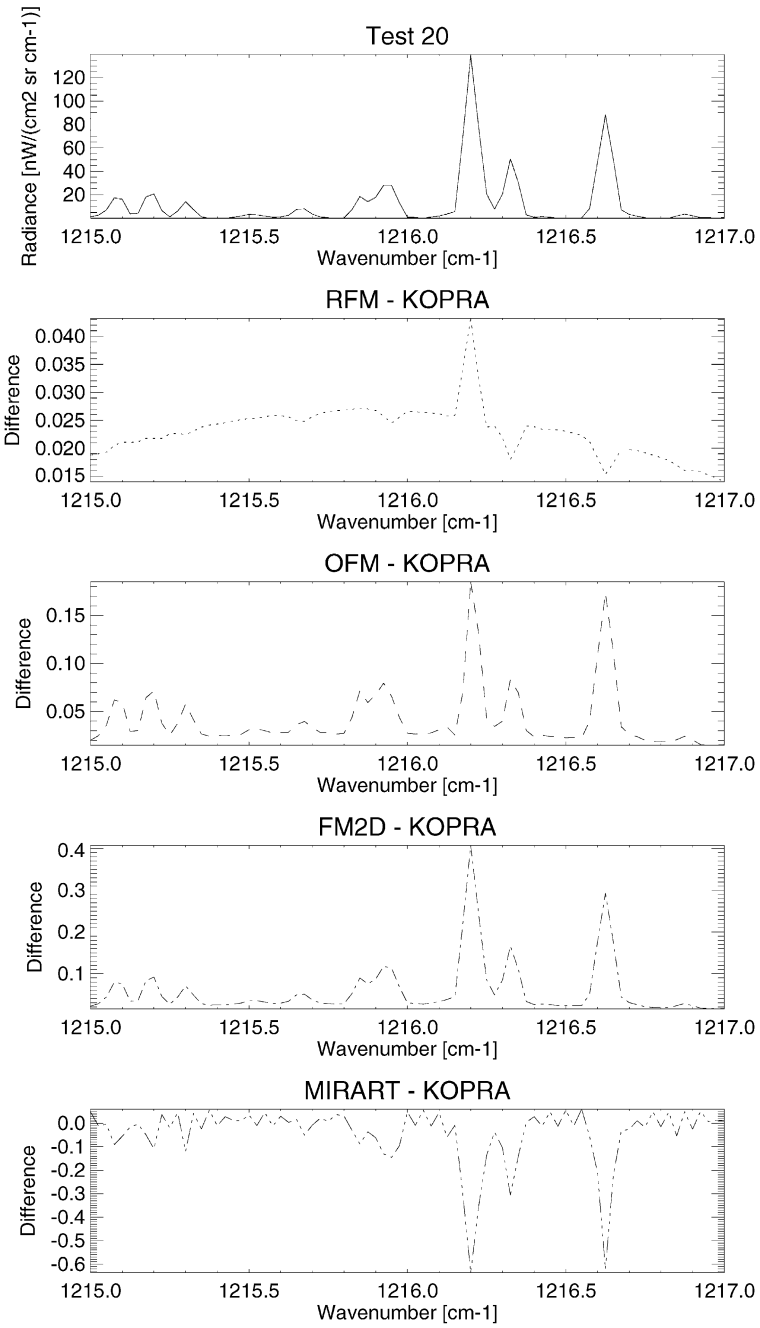

Fig. 9. FOV-convolved radiance spectra (test case 20). The uppermost panel shows the spectra for all codes (not distinguishable from each other), whereas the other panels show difference spectra with respect to KOPRA.

interpolation. Laboratory measurements of these cross sections have been provided by Varanasi. These are an extension to the data set described in Ref. [49].

Most pronounced residuals between RFM and KOPRA spectra are in the high wavenumber slopes of the Q-branches (Fig. 10). These are explained by different interpolation approaches of absorption cross sections in pressure and temperature. These differences are even amplified when the instrument field of view is considered. Differences between the IROE1 and KOPRA spectra are smaller.

4.11. Non-local thermodynamic equilibrium

The purpose of test cases 27–30 was assessment of non-local thermodynamic equilibrium (non-LTE) modelling on the basis of precalculated vibrational temperatures. While the microwindow used in test cases 27 and 28 actually lies outside the MIPAS band, the spectral intervals used here have been chosen to allow comparison to a joint activity of the International Radiation Commission (IRC), where further radiative transfer models were investigated for non-LTE conditions [53]. The only codes under investigation here, which support non-LTE, are RFM and KOPRA. As already found during the IRC activities, there is no evidence of non-LTE related discrepancies in radiative transfer modelling between RFM and KOPRA.

5. Conclusion

The intercomparison experiment was quite enlightening for all participants. The overall interconsistency of spectra is good, except for test cases where functionalities were required which were beyond the specification of some of the codes, e.g. line coupling, non-local thermodynamic equilibrium, etc. Some differences in details are caused by different implementations of the Voigt line shape and related approximations. Different approaches to calculate the line intensity as a function of temperature lead to noticeably different spectra. Consideration of atmospheric refraction, line mixing, pressure shift, self-broadening and non-local thermodynamic equilibrium turned out to be important in some cases. Considerable differences, however, were caused by different settings of parameters driving the numerical accuracy: the layering of the atmosphere used for integration of the radiative transfer equation as well as the number of pencil beams used for the field of view convolution seem to be of particular importance for reliable results. While all codes proved reliable within their specification, the trade-off between accuracy and computational efficiency still is a major issue, since input parameter settings which lead to more accurate results lead to extended computational effort which may in some cases not be tolerable for operational use. This is in particular true for the integration of the radiance field over the instrument field of view.

Acknowledgements

AMIL2DA is a Shared Cost Action within the RTD generic activities of the 5th FP EESD Programme of the European Commission, Project EVG1-CT-1999-00015. M.L.-P. has been partially supported by PNE under contract PNE-017/2000-C. P. Varanasi gave access to spectroscopic

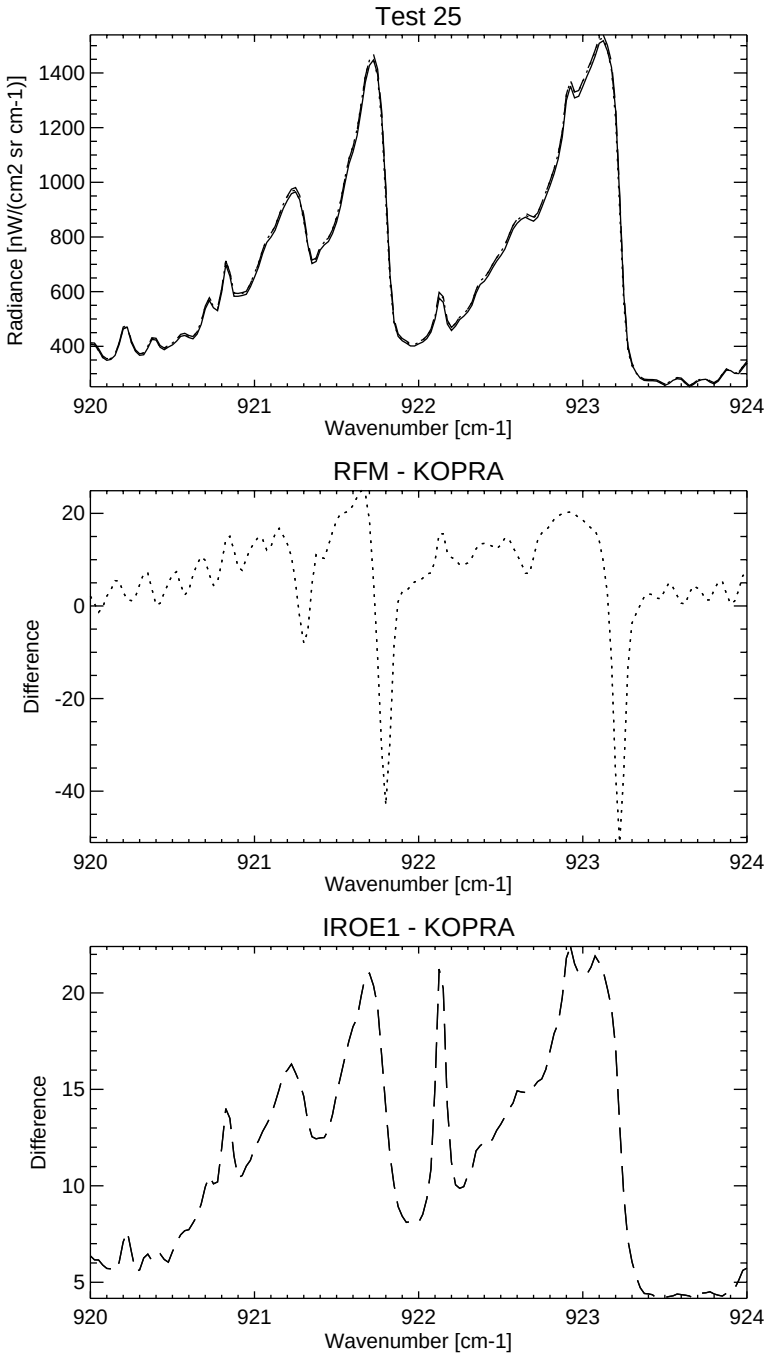

Fig. 10. Emission spectra of CFC-12 (test case 25). The uppermost panel includes the spectra (KOPRA: solid; RFM: dotted; IROE1: long dashes). The other panels show difference spectra with respect to KOPRA.

cross-section data prior to their publication in HITRAN. Furthermore thanks go to J.-M. Flaud and G. Schwarz, who provided helpful comments to the manuscript.

References

[1] Endemann M, Fischer H. Envisat's high-resolution limb sounder: MIPAS. ESA Bull 1993;76:47–52.
[2] Endemann M, Gare P, Smith D, Hoerning K, Fladt B, Gessner R. MIPAS design overview and current development status. In: Proceedings EUROPTO series, Optics in Atmospheric Propagation, Adaptive Systems, and Lidar Techniques for Remote Sensing, Taormina, Italy, 24–26 September, vol. 2956, 1996. p. 124–35.
[3] Fischer H, Oelhaf H. Remote sensing of vertical profiles of atmospheric trace constituents with MIPAS limb emission spectrometers. In: Wang J, Wu B, Ogawa T, Guan Z, editors. Optical remote sensing of the atmosphere and clouds, Beijing, China, 15–17 September 1998; Proc SPIE 1998;3501:42–6.
[4] Fischer H, Anderson GP, von Clarmann T, Clough SA, Coffey MT, Goldman A, Kneizys FX. Intercomparison of transmittance and radiance algorithms (ITRA). Report of the limb-group of the ITRA-workshop at the University of Maryland, 12–14 March 1986, Wissenschaftliche Berichte KfK 4349, Kernforschungszentrum Karlsruhe, 1988.
[5] Sherlock VJ. Results from the first UKMO IASI radiative transfer model intercomparison. Technical Report, Numerical Weather Prediction Division, 2000. Technical Report No. 287.
[6] Garand L, Turner DS, Larocque M. Intercomparison of radiative transfer codes applied to HIRS and AMSU channels. In: Smith WL, Timofeyev YM, editors. RS 2000: current problems in atmospheric radiation. Hampton, VA, USA: A. Deepak Publishing, 2001. p. 64–5.
[7] Chandrasekhar S. Radiative transfer. New York: Dover Publications Inc., 1960.
[8] Edlen B. The refractive index of air. Metrologia 1966;2:71–80.
[9] Curtis AR. A statistical model for water-vapour absorption. Q J R Meteorol Soc 1952;78:638–40.
[10] Godson WL. The evaluation of infra-red radiative fluxes due to atmospheric water vapour. Q J R Meteorol Soc 1953;79:367–79.
[11] Godson WL. The computation of infrared transmission by atmospheric water vapour. J Meteorol 1955;12:272–84.
[12] Curtis AR. The computation of radiative heating rates in the atmosphere. Proc R Soc London Ser A 1956;236: 156–9.
[13] Stiller GP, editor, The Karlsruhe optimized and precise radiative transfer algorithm (KOPRA), vol. FZKA 6487, Wissenschaftliche Berichte, Forschungszentrum Karlsruhe, 2000.
[14] Stiller GP, von Clarmann T, Funke B, Glatthor N, Hase F, Höpfner M, Linden A. Sensitivity of trace gas abundances retrievals from infrared limb emission spectra to simplifying approximations in radiative transfer modelling. JQSRT 2002;72:249–80.
[15] Schreier F, Schimpf B. A new efficient line-by-line code for high resolution atmospheric radiation computations incl. derivatives. In: Smith WL, Timofeyev Y, editors. IRS 2000: current problems in atmospheric radiation. Hampton, VA, USA: A. Deepak Publishing, 2002. p. 381–4.
[16] Ridolfi M, Carli B, Carlotti M, von Clarmann T, Dinelli B, Dudhia A, Flaud J-M, Höpfner M, Morris PE, Raspollini P, Stiller G, Wells RJ. Optimized forward and retrieval scheme for MIPAS near-real-time data processing. Appl Opt 2000;39(8):1323–40.
[17] Hase F, Höpfner M. Atmospheric ray path modelling for radiative transfer algorithms. Appl Opt 1999;38(15): 3129–33.
[18] Kuntz M. A new implementation of the Humlicek algorithm for the calculation of the Voigt profile function. JQSRT 1997;57(6):819–24.
[19] Humlicek J. Optimized computation of the Voigt and complex probability functions. JQSRT 1982;27(4):437–44.
[20] Cousin C, Le Doucen R, Boulet C, Henry A. Temperature dependence of the absorption in the region beyond the 4.3-μm band head of CO_2. 2: N_2 and O_2 broadening. Appl Opt 1985;24(22):3899–907.
[21] Le Doucen R, Cousin C, Boulet C, Henry A. Temperature dependence of the absorption in the region beyond the 4.3-μm band head of CO_2. 1: Pure CO_2 case. Appl Opt 1985;24(6):897–906.
[22] Menoux V, Le Doucen R, Boissoles J, Boulet C. Line shape in the low frequency wing of self- and N_2-broadened v_3 CO_2 lines: temperature dependence of the asymmetry. Appl Opt 1991;30(3):281–6.

[23] Funke B, Stiller GP, von Clarmann T, Echle G, Fischer H. CO_2 line mixing in MIPAS limb emission spectra and its influence on retrieval of atmospheric parameters. JQSRT 1998;59(3–5):215–30.
[24] Rosenkranz P. Pressure broadening of rotational bands. I. A statistical theory. J Chem Phys 1985;83(12):6139–44.
[25] Clough SA, Kneizys FX, Davies RW. Line shape and the water vapor continuum. Atmos Res 1989;23:229–41.
[26] Carli B, Ridolfi M, Raspollini P, Dinelli BM, Dudhia A, Echle G. Study of the retrieval of atmospheric trace gas profiles from infrared spectra. Technical Report, European Space Agency, 1998, Final Report of ESA Contract 12055/96/NL/CN.
[27] Höpfner M, Oelhaf H, Wetzel G, Friedl-Vallon F, Kleinert A, Lengel A, Maucher G, Nordmeyer H, Glatthor N, Stiller GP, von Clarmann T, Fischer H, Kröger C, Deshler T. Evidence of scattering of tropospheric radiation by PSCs in mid-IR limb emission spectra: MIPAS-B observations and KOPRA simulations. Geophys Res Lett 2002; 29(8).
[28] Kuntz M, Höpfner M. Efficient line-by-line calculation of absorption coefficients. JQSRT 1999;63(1):97–114.
[29] Edwards DP, GENLN2: A general line-by-line atmospheric transmittance and radiance model. Technical Report, NCAR, Boulder, Colorado, 1992. Version 3.0, Description and users guide, NCAR/TN-367+STR.
[30] Clough SA, Kneizys FX, Shettle EP, Anderson GP. Atmospheric radiance and transmittance: FASCOD2. In: Proceedings of the Sixth Conference on Atmospheric Radiation, American Meteorological Society, Williamsburg, VA, May 1986. p. 141–6.
[31] Rothman LS, Rinsland CP, Goldman A, Massie T, Edwards DP, Flaud J-M, Perrin A, Camy-Peyret C, Dana V, Mandin J-Y, Schroeder J, McCann A, Gamache RR, Wattson RB, Yoshino K, Chance KV, Jucks KW, Brown LR, Nemtchinov V, Varanasi P. The HITRAN molecular spectroscopic database and HAWKS (HITRAN atmospheric workstation): 1996 edition. JQSRT 1998;60:665–710.
[32] Strow LL, Motteler HE, Benson RG, Hannon SE, De Souza-Machado S. Fast computation of monochromatic infrared atmospheric transmittances using compressed look-up tables. JQSRT 1998;59(3–5):481–93.
[33] Dudhia A, Morris PE, Wells RJ. Fast monochromatic radiative transfer calculations for limb sounding. JQSRT 2002;74:745–56.
[34] Wells RJ. Rapid approximation to the Voigt/Faddeeva function and its derivatives. JQSRT 1999;62(1):29–48.
[35] Clough SA, Iacono MJ, Moncet JL. Line-by-line calculations of atmospheric fluxes and cooling rates: application to water vapor. J Geophys Res 1992;97:15761–86.
[36] Schimpf B, Schreier F. Robust and efficient inversion of vertical sounding atmospheric high-resolution spectra by means of regularization. J Geophys Res 1997;102(D13):16,037–55.
[37] Hui AK, Armstrong BH, Wray AA. Rapid computation of the Voigt and complex error functions. JQSRT 1978;19: 509–16.
[38] Schreier F. The Voigt and complex error function: a comparison of computational methods. JQSRT 1992;48(5/6): 743–62.
[39] Rothman LS, Wattson RB, Gamache RR, Schroeder J, McCann A. HITRAN HAWKS and HITEMP high temperature molecular databases. Proc SPIE 1995;2471:105–11.
[40] Chance KV, Jucks KW, Johnson DG, Traub WA. The Smithsonian astrophysical observatory database 1992. JQSRT 1994;52:447–57.
[41] Jacquinet-Husson N, Arié E, Ballard J, Barbe A, Bjoraker G, Bonnet B, Brown LR, Camy-Peyret C, Champion JP, Chédin A, Chursin A, Clerbaux C, Duxbury G, Flaud J-M, Fourrié N, Fayt A, Graner G, Gamache R, Goldman A, Golovko V, Guelachvili G, Hartmann JM, Hilico JC, Hillman J, Lefèvre G, Lellouch E, Mikhaïlenko SN, Naumenko OV, Nemtchinov V, Newnham DA, Nikitin A, Orphal J, Perrin A, Reuter DC, Rinsland CP, Rosenmann L, Rothman LS, Scott NA, Selby J, Sinitsa LN, Sirota JM, Smith AM, Smith KM, Tyuterev VG, Tipping RH, Urban S, Varanasi P, Weber M. The 1997 spectroscopic GEISA databank. JQSRT 1999;62(2):205–54.
[42] Pickett HM, Poynter RL, Cohen EA, Delitsky ML, Pearson JC, Müller HSP. Submillimeter, millimeter, and microwave spectral line catalog. JQSRT 1998;60(5):883–90.
[43] Norton RH, Rinsland CP. ATMOS data processing and science analysis methods. Appl Opt 1991;30(4):389–400.
[44] Liebe HJ, Hufford GA, Cotton MG. Propagation modeling of moist air and suspended water/ice particles at frequencies below 1000 GHz. In: Proceedings of the 52nd Specialists Meeting of the Electromagnetic Wave Propagation Panel, AGARD, May 1993.
[45] Kahaner D, Moler C, Nash S. Numerical methods and software. Englewood Cliffs, NJ: Prentice-Hall, 1989.

[46] Ridolfi M, Hoepfner M, Raspollini P. Implementation of the Voigt line-shape calculation in the forward model for operational MIPAS retrievals. In: Zoppi M, Ulivi L, editors. Proceedings of the 13th ICSLS, Florence, Italy: AIP Press, vol. 9, 1997. p. 126–31.

[47] Norton H, Beer R. New apodizing functions for Fourier spectrometry. J Opt Soc Am 1976;66(3):259–64 (Errata J Opt Soc Am 1977;67:419).

[48] Reburn WJ, Siddans R, Kerridge BJ, Buehler S, von Engeln A, Eriksson P, Kuhn-Sander T, Kuenzi K, Verdas C. Critical assessments in millimetre-wave atmospheric limb sounding. Final Report, ESA Contract No.: 13348/98/NL/GD, Part V.

[49] Varanasi P, Nemtchinov V. Thermal infrared absorption coefficients of CFC-12 at atmospheric conditions. JQSRT 1994;51(5):679–87.

[50] López-Puertas M, Zaragoza G, López-Valverde MÁ, Martín-Torres FJ, Shved GM, Manuilowa RO, Kutepov AA, Gusev O, von Clarmann T, Linden A, Stiller G, Wegner A, Oelhaf H, Edwards DP, Flaud J-M. Non-local thermodynamic equilibrium limb radiances for the MIPAS instrument on ENVISAT-1. JQSRT 1998;59(3–5): 377–403.

[51] Hase F, Transformation of irradiated to measured spectral distribution due to finite spectral resolution and field of view extent of a Fourier transform spectrometer. In: Stiller GP, editor. The Karlsruhe Optimized and Precise Radiative transfer Algorithm (KOPRA), Wissenschaftliche Berichte FZKA 6487, Forschungszentrum Karlsruhe, 2000. p. 119–32.

[52] Strow LL, Tobin DC, Hannon SE. A compilation of first-order line-mixing coefficients for CO_2 Q-branches. JQSRT 1994;52(3/4):281–94.

[53] von Clarmann T, Dudhia A, Edwards DP, Funke B, Höpfner M, Kerridge B, Kostsov V, Linden A, López-Puertas M, Timofeyev Y. Intercomparison of radiative transfer codes under non-local thermodynamic equilibrium conditions. J Geophys Res 2002, accepted for publication.